

Charge-to-Spin Interconversion in Low-Symmetry Topological Materials

Marc Vila,^{1,2} Chuang-Han Hsu,³ Jose H. Garcia,¹ L. Antonio Benítez,^{1,2}
Xavier Waintal,⁴ Sergio Valenzuela,^{1,5} Vitor M. Pereira,⁶ and Stephan Roche^{1,5}

¹*Catalan Institute of Nanoscience and Nanotechnology (ICN2),
CSIC and BIST, Campus UAB, Bellaterra, 08193 Barcelona, Spain*

²*Department of Physics, Universitat Autònoma de Barcelona,
Campus UAB, Bellaterra, 08193 Barcelona, Spain*

³*Department of Electrical and Computer Engineering,
National University of Singapore, Singapore 117576, Singapore*

⁴*Univ. Grenoble Alpes, CEA, IRIG-PHELIQS, 38000 Grenoble, France*

⁵*ICREA–Institució Catalana de Recerca i Estudis Avançats, 08010 Barcelona, Spain*

⁶*Centre for Advanced 2D Materials and Graphene Research Centre,
National University of Singapore, Singapore 117546, Singapore*

(Dated: December 22, 2024)

The spin polarization induced by the spin Hall effect (SHE) in thin films typically points out of the plane. This is rooted not in a fundamental constraint but on the specific symmetries of traditionally studied systems. We theoretically show that the reduced symmetry of strong spin-orbit coupling materials such as MoTe₂ or WTe₂ enables new forms of intrinsic SHE that produce large and robust in-plane spin polarizations. Through quantum transport calculations on realistic device geometries with disorder, we show that the charge-to-spin interconversion efficiency can reach $\theta_{xy} \approx 80\%$ and is gate tunable. The numerically extracted spin diffusion lengths (λ_s) are long and yield large values of the figure of merit $\lambda_s \theta_{xy} \sim 8\text{--}10$ nm, largely superior to conventional SHE materials. These findings vividly emphasize how crystal symmetry governs the intrinsic SHE, and how it can be exploited to broaden the range and efficiency of spintronic functionalities. Specific guidelines for their experimental confirmation are proposed.

Unconventional manifestations of spin-orbit coupling (SOC) are rapidly extending the ability to generate, control and carry spin polarization for applications involving spin transport or spin-driven magnetic torques beyond conventional spintronic materials [1, 2]. Topological materials are a natural family to scrutinize in this regard: their key features often derive from a large SOC combined with band inversions, and their topologically protected surface states may prove instrumental to enable coherent, dissipationless spin currents over long-distances [3]. 3D Weyl semimetals (WSM) are defined by the presence of band degeneracy points (Weyl nodes) near the Fermi energy (E_F) with local linear dispersion in all directions [4, 5]. Momentum-separated pairs of bulk Weyl nodes with opposite Berry flux “charge” are topologically stable and determine the existence of Fermi arc surface states [6–10].

Layered transition metal dichalcogenides (TMDs) in the 1T' ($P2_1/m$) or 1T_d ($Pmn2_1$) phases accommodate the interesting class of WSM candidates MX₂ (M = Mo, W; X = S, Se, Te), which have been advanced as platforms for realizing exotic phenomena such as topological superconductivity [11–13], non-linear Hall effect [14–16], anisotropic spin Hall transport [17] or out-of-plane spin-orbit torque [18]. When thinned towards the monolayer limit, they exhibit a transition from the type-II WSM behavior characteristic of the bulk to the quantum spin Hall regime [6–10, 19–27]. Recent experiments reported the generation of large charge-to-spin interconversion (CSI) by the SHE in multilayers of MoTe₂ and

WTe₂ [28, 29]. In parallel, nonlocal measurements of spin transport extracted anomalously long spin diffusion lengths ($\lambda_s \sim 1 \mu\text{m}$) in MoTe₂ at room temperature, as well as an unconventional SHE that produces spins colinear with the charge current [30].

The efficiency of the SHE is captured by the spin Hall angle (SHA, θ_{xy}) which indicates which percentage of spin current is produced for a driving charge current; θ_{xy} strongly depends on the strength of SOC at play in the material and is usually no more than a few percent at room temperature in heavy metals [31]. Additionally, the stronger the SOC, the shorter λ_s is, and achieving long λ_s concurrently with large SHA is a long-standing challenge for spintronics, which is also dependent on the underlying dominant mechanism at play. Indeed, SHE encompasses two different types of contributions, namely a purely bandstructure-driven intrinsic part which coexists with an extrinsic part generated by disorder and impurity scattering [32], and to date the best tradeoff obtained for heavy metals amounts to $\lambda_s \theta_{xy} \sim 0.1\text{--}0.2$ nm [31, 33–36]. In this regard, the higher structural quality and resilience to disorder of topological materials such as MoTe₂ or WTe₂ could correspond to large SHE efficiency primarily driven by a strong SOC and intrinsic spin Hall conductivity (SHC), but to date the spintronic potential of these low-symmetry topological material has not yet been clarified.

In this Letter, we show that unique symmetry-induced spin textures of electronic states in MoTe₂ and WTe₂ monolayers yield a *giant oblique SHE*, that is, a SHE

where spins lie in the yz plane. We obtained CSI efficiencies as high as 80% and values of λ_s in the range 10–100 nm; the latter are one order of magnitude larger than in heavy metals with similar spin Hall efficiency [31]. Additionally, all spin transport characteristics are gate-tunable, being maximal near the band edge. Our findings hinge on a newly DFT-derived effective tight-binding model deployed in spintronic simulations using state-of-the-art quantum transport methodologies. While there have been recent theoretical characterizations of the SOC and SHC in pristine forms of these materials [17, 30], deeper fundamental understanding of the spin dynamics and transport remains pressing, while realistic assessment of the length scales associated with spin transport is paramount for further experimental scrutiny and practical applications. We address those questions here.

Electronic Model. We computed the bandstructures of $1T'$ - and $1T_d$ -derived monolayers of MoTe_2 and WTe_2 within density functional theory (DFT), as described in the supplemental material [37]. Effective Hamiltonians based on maximally localized Wannier functions were subsequently extracted, which allow straightforward computation of the SHC and spin textures with no intervening approximations. Yet, such Hamiltonian is still too complex to efficiently deploy in large-scale on a real-space transport calculation. We therefore developed a $\mathbf{k}\cdot\mathbf{p}$ Hamiltonian to describe the two conduction and two valence bands nearest E_F which, at Γ , respectively transform according to the representations B_u (valence) and A_g (conduction) of the point group C_{2h} [21]. Extension of the symmetry-allowed $\mathbf{k}\cdot\mathbf{p}$ terms to the full Brillouin zone yields the following nearest-neighbor tight-binding representation in real space [37]:

$$\begin{aligned}
H = & \sum_{i,s} (\Delta + 4m_d + \delta) c_{i,s}^\dagger c_{i,s} - \sum_{\langle ij \rangle, s} (m_p + m_d) c_{i,s}^\dagger c_{j,s} \\
& + \sum_{i,s} (\Delta - 4m_d - \delta) d_{i,s}^\dagger d_{i,s} - \sum_{\langle ij \rangle, s} (m_p - m_d) d_{i,s}^\dagger d_{j,s} \\
& - \sum_{\langle ij \rangle, s} \frac{\beta}{2} (\hat{l}_{ij} \cdot \hat{\mathbf{y}}) c_{i,s}^\dagger d_{j,s} + \sum_{i,s} \eta c_{i,s}^\dagger d_{i,s} \\
& - \sum_{\langle ij \rangle} \sum_{ss'} \frac{i}{2} (\boldsymbol{\Lambda}_{ss'} \times \hat{l}_{ij}) \cdot (\hat{\mathbf{y}} + \hat{\mathbf{z}}) c_{i,s}^\dagger d_{j,s'}. \quad (1)
\end{aligned}$$

This is an effective 4-band Hamiltonian generated by two orbitals (plus spin) per unit cell on a rectangular lattice, one arising from the p_y states of the chalcogens and the other from d_{yz} of the metal ion, respectively described by the $c_{i,s}$ and $d_{i,s}$ operators at each unit cell i (s labels the spin projection). The first two lines in Eq. (1) describe spin-degenerate valence and conduction bands with hopping amplitudes set by $m_p \pm m_d$, δ parameterizes the degree of band inversion at Γ , and a constant Δ is used to match the position of the conduction band and E_F with those obtained by DFT. In the third line, β accounts for the x - y crystalline anisotropy, with \hat{l}_{ij}

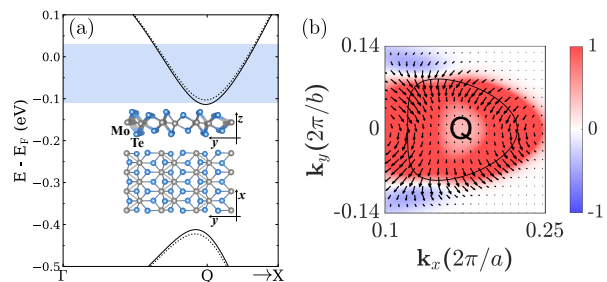


FIG. 1. (a) Close-up of the bandstructure near E_F according to the 4-band tight-binding model for a T_d - MoTe_2 monolayer. The blue-shaded region indicates the energy range covered in the spin transport calculations. Inset: monolayer crystal structure. (b) Spin texture of one of the bands of the electron pocket near Q at E_F (Fermi-broadened with $T = 300$ K); the solid line marks the Fermi contour, arrows depict the in-plane spin projection and the color scale the spin projection along $\hat{\mathbf{z}}$.

a unit vector pointing from site i to j ; the term $\propto \eta$ breaks inversion symmetry and determines, for example, whether we are describing a monolayer descended from a $1T'$ ($\eta = 0$) or $1T_d$ bulk crystal [38]. The last line embodies the SOC, where $\boldsymbol{\Lambda} \equiv (\Lambda_x \sigma_x, -\Lambda_y \sigma_y, \Lambda_z \sigma_z)$, $\sigma_{x,y,z}$ are the spin Pauli matrices and $\hat{\mathbf{y}}, \hat{\mathbf{z}}$ are unit Cartesian vectors.

The parameters are set by fitting the energy dispersion and spin texture to the ones obtained by DFT [37]. To be specific, we shall henceforth concentrate on the case of MoTe_2 , as it is the one where experiments have recently reported in-plane SHE [28, 30]. The model (1) captures equally well the case of WTe_2 and similar low symmetry TMDs [37]. Since the DFT calculations show that MoTe_2 is slightly n -doped at room temperature, we favored the conduction band in the fits and will henceforth focus exclusively on cases where E_F lies in the conduction band. The band structure near E_F according to (1) is shown in Fig. 1a. The valence and conduction band extrema present a small splitting and occur at the time-reversal-symmetric Q point. Fig. 1b shows the spin texture at the Fermi energy, $\langle s^\alpha \rangle_{E_F}$. An important observation from this plot is that the spin texture is characterized by $\langle s^y \rangle_{E_F} > \langle s^z \rangle_{E_F} \gg \langle s^x \rangle_{E_F}$, in line with prior results [16, 39].

Spin transport. We explored the spin transport properties of this model using linear response theory and the Landauer-Büttiker transport formalism as implemented in Kwant [40]. We simulated the nonlocal spin valve illustrated in the inset of Fig. 2, where contacts 2 and 3 are ferromagnetic (FM) to allow injection and detection of spin-polarized currents [41–43]: FM electrode 2 injects a spin-polarized current I_0^α with spins polarized along $\alpha \in \{x, y, z\}$; this creates a spin accumulation that diffuses along the channel and is detected as a nonlocal voltage V_{nl} at electrodes 3-4, located a distance L from the

T_d -phases [30]. The central aspect in that case is that, while only the conventional SHE is allowed by symmetry in bulk crystals of T_d type, reduction to few-layer slabs removes the glide mirror symmetries along the stacking direction; the lower symmetry allows for additional non-zero components of the SHC tensor, or SHA (θ_{ij}^α) as defined above [30]. The results in Fig. 3 represent the expected behavior in the extreme monolayer limit. Interestingly, note that the spin accumulation displays the hierarchy $s^y > s^z > s^x$, echoing the trend seen above for the spin texture and spin diffusion lengths.

We determine θ_{xy}^α by fitting the numerically calculated spin accumulation to Eq. (2), using the values of D_s extracted from the two-terminal conductance of this device and λ_s^α from Fig. 2 [37]. The results are displayed in the inset of Fig. 3. We note that while the charge conductivity along x and y is slightly anisotropic, resulting in an equally anisotropic SHA, $|\theta_{xy}^\alpha|$ and $|\theta_{yx}^\alpha|$ are still very similar [37]. At E_F , the SHA for spins pointing along y and z have magnitudes of $\approx 10\%$ (but opposite sign). Remarkably, both increase substantially when approaching the band edge, at which point $|\theta_{xy}^y|$ overcomes $|\theta_{xy}^z|$ with values as large as $|\theta_{xy}^y| \approx 83\%$. To validate these results, we compute the SHC and the SHA with the Kubo formula (see Fig. 8 in supplemental material [37]), and obtain the same trends both qualitatively and quantitatively. This increase of θ_{xy} is qualitatively consistent with the presence of hotspots of spin-Berry curvature near the bottom of the electron pockets [30], which determine the magnitude of the SHC/SHA [17, 45, 46]. Importantly, our combined results yield CSI efficiencies with $\lambda_s\theta_{xy} \sim 8\text{--}10$ nm, which is much larger than in traditional SOC materials (Pt, β -W, β -Ta or Au) for which $\lambda_s\theta_{xy} \sim 0.1\text{--}0.2$ nm [31, 34, 47], and 2 to 3 times larger than that induced by proximity in graphene [48].

Spin precession. Such a peculiar spin response should become manifest in suitably designed nonlocal spin-precession experiments [28, 48, 49]. To anticipate the experimental signature of this oblique SHE, we propose the device concept pictured in the insets of Fig. 4, which relies on the reciprocal/inverse SHE (ISHE) [31]. It consists of a Hall bar comprising a graphene channel and a transversely aligned monolayer TMD crystal. A non-equilibrium spin accumulation is induced in the graphene channel through a FM electrode whose magnetization direction determines that of the spin density injected into graphene underneath. This spin accumulation generates a pure-spin current that diffuses toward—and is absorbed by—the remote TMD. It is assumed that the spin current is absorbed by the TMD at its edge and continues to follow the diffusion direction, given that the spin resistance in the TMD is two orders of magnitude lower than in graphene for $\lambda_s^y = 35$ nm or $\lambda_s^z = 12$ nm [37]. By ISHE, a transverse voltage V_{ISHE} develops on the TMD, which can be measured along its length as illustrated in Fig. 4. In experiments, the diffusing spins can be rou-

tinely controlled by an external magnetic field \mathbf{B} which, if non-colinear with the FM, drives a controlled spin precession. To capture this situation, we generalized the Bloch diffusion equations to account for anisotropic spin diffusion and calculated $V_{\text{ISHE}}(\mathbf{B})$ using the approach described in Ref. 48 (which accurately reproduces CSI in real devices). Fig. 4 shows the precession response for two selected orientations of the TMD crystal in the limit of full absorption ($R_{\text{ISHE}} \equiv V_{\text{ISHE}}/I_0^y$) [37]. We observe magnitudes of R_{ISHE} nearly three orders of magnitude larger than the values reported for graphene/WS₂, graphene/MoS₂ [48, 50, 51], and graphene/bulk-WSMs [28, 29]. This is a direct consequence of the extremely large SHAs predicted here for MoTe₂ [52].

The essence of the experiment is that the precession response depends strongly on the crystal orientation. As evidenced in Fig. 2, the spin relaxation in the TMD is anisotropic, and the CSI depends crucially on both the majority spin orientation and crystalline orientation. In Fig. 4(a), the TMD’s crystallographic y -axis is transverse to the spin propagation. A magnetic field parallel to \hat{z} causes spins to precess in the graphene plane but, according to Fig. 3, only the y spin projection contributes to the ISHE signal with an efficiency of $|\theta_{xy}^y|$; R_{ISHE} is symmetric with respect to the sign of B because the magnetization at the FM injector is parallel to y , resulting in the maximum signal at $B = 0$. When the field is parallel to \hat{x} , the spins acquire a z component (in addition to that in y), which is asymmetric with respect to B and adds a contribution to the ISHE with an efficiency of $|\theta_{xy}^z|$; because $|\theta_{xy}^y| \simeq 2|\theta_{xy}^z|$, the signal remains roughly symmetric. In Fig. 4(b), the crystallographic y -axis is parallel to the spin propagation. As the y and z directions are now orthogonal to the FM magnetization, the lineshapes are antisymmetric. The signal is zero at $B = 0$ and, as the B is swept from negative to positive along \hat{z} (\hat{x}), the spin component along y (z) changes sign. Therefore, two combined observations in this proposed experiment represent a “smoking gun” demonstration of the intrinsic oblique SHE predicted in this work: (i) $R_{\text{ISHE}}(B)$ should display a different lineshape under different field orientations for a fixed TMD crystal; (ii) rotation of the crystal converts the lineshapes from predominantly symmetric to antisymmetric.

Conclusion. Numerical calculations for 1T'- and 1T_d-derived monolayers of TMDs such as MoTe₂ or WTe₂, reveal that the spin transport length scales in these systems reflect the peculiar spin textures that materialize as a result of reduced symmetry and strong SOC. The extracted charge-to-spin interconversion figure of merit $\lambda_s\theta_{xy} \sim 8\text{--}10$ nm is up to two orders of magnitude superior than in other actively scrutinized materials such as Pt, Au, W, and Ta [31, 34]. Our findings also call for a careful analysis of SHE measurements, since the interpretation of all-electrical detection in Hall bars [30, 53, 54] usually ignores the possibility of multiple spin Hall com-

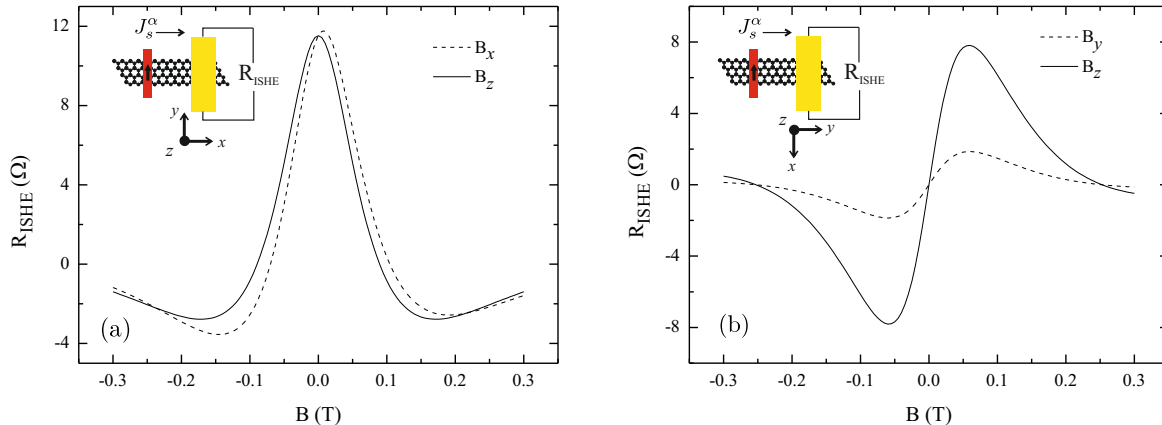


FIG. 4. Simulated response of the inverse SHE (R_{ISHE}) to spin precession for two orientations of the TMD crystal (coordinate axes in the insets). The device geometry is shown in the insets, with the TMD depicted in yellow and the FM injector in red (magnetization indicated by an arrow). The polarization of the spin current reaching the TMD (J_s^α) is controlled externally with a magnetic field, \mathbf{B} , oriented either along the graphene channel (dashed lines) or out-of-plane (solid lines). Typical experimental device dimensions were used in the simulation [37].

ponents. We show how the presence of oblique SHE can be experimentally identified by reciprocal SHE, and how the different SHC contributions may be isolated in a spin precession setup.

M.V. acknowledges support from “La Caixa” Foundation and the Centre for Advanced 2D Materials at the National University of Singapore for its hospitality. X. W. acknowledges the ANR Flagera GRANSPOUR funding. ICN2 authors were supported by the European Union Horizon 2020 research and innovation programme under Grant Agreement No. 785219 (Graphene Flagship) and No. 824140 (TOCHA, H2020-FETPROACT-01-2018). ICN2 is funded by the CERCA Programme/Generalitat de Catalunya, and is supported by the Severo Ochoa program from Spanish MINECO (Grant No. SEV-2017-0706 and MAT2016-75952-R). V.M.P. acknowledges the support of the National Research Foundation (Singapore) under its Medium-Sized Centre Programme (R-723-000-001-281).

[1] W. Han, Y. Otani, and S. Maekawa, *npj Quantum Mater.* **3**, 27 (2018).
 [2] A. Manchon, J. Železný, I. M. Miron, T. Jungwirth, J. Sinova, A. Thiaville, K. Garello, and P. Gambardella, *Rev. Mod. Phys.* **91**, 035004 (2019).
 [3] Y. Fan and K. L. Wang, *SPIN* **06**, 1640001 (2016).
 [4] A. A. Burkov and L. Balents, *Phys. Rev. Lett.* **107**, 127205 (2011).
 [5] X. Wan, A. M. Turner, A. Vishwanath, and S. Y. Savrasov, *Phys. Rev. B* **83**, 205101 (2011).

[6] A. A. Soluyanov, D. Gresch, Z. Wang, Q. Wu, M. Troyer, X. Dai, and B. A. Bernevig, *Nature* **527**, 495 (2015).
 [7] Y. Sun, S.-C. Wu, M. N. Ali, C. Felser, and B. Yan, *Phys. Rev. B* **92**, 161107 (2015).
 [8] S.-Y. Xu, I. Belopolski, N. Alidoust, M. Neupane, G. Bian, C. Zhang, R. Sankar, G. Chang, Z. Yuan, C.-C. Lee, S.-M. Huang, H. Zheng, J. Ma, D. S. Sanchez, B. Wang, A. Bansil, F. Chou, P. P. Shibayev, H. Lin, S. Jia, and M. Z. Hasan, *Science* **349**, 613 (2015).
 [9] J. Jiang, Z. K. Liu, Y. Sun, H. F. Yang, C. R. Rajamathi, Y. P. Qi, L. X. Yang, C. Chen, H. Peng, C.-C. Hwang, S. Z. Sun, S.-K. Mo, I. Vobornik, J. Fujii, S. S. P. Parkin, C. Felser, B. H. Yan, and Y. L. Chen, *Nature Communications* **8**, 13973 (2017).
 [10] P. Li, Y. Wen, X. He, Q. Zhang, C. Xia, Z.-M. Yu, S. A. Yang, Z. Zhu, H. N. Alshareef, and X.-X. Zhang, *Nature Communications* **8**, 2150 (2017).
 [11] Y. Qi, P. G. Naumov, M. N. Ali, C. R. Rajamathi, W. Schnelle, O. Barkalov, M. Hanfland, S.-C. Wu, C. Shekhar, Y. Sun, V. Süß, M. Schmidt, U. Schwarz, E. Pippel, P. Werner, R. Hillebrand, T. Förster, E. Kampert, S. Parkin, R. J. Cava, C. Felser, B. Yan, and S. A. Medvedev, *Nature Communications* **7**, 11038 (2016).
 [12] V. Fatemi, S. Wu, Y. Cao, L. Bretheau, Q. D. Gibson, K. Watanabe, T. Taniguchi, R. J. Cava, and P. Jarillo-Herrero, *Science* **362**, 926 (2018).
 [13] E. Sajadi, T. Palomaki, Z. Fei, W. Zhao, P. Bement, C. Olsen, S. Luescher, X. Xu, J. A. Folk, and D. H. Cobden, *Science* **362**, 922 (2018).
 [14] Q. Ma, S.-Y. Xu, H. Shen, D. MacNeill, V. Fatemi, T.-R. Chang, A. M. Mier Valdivia, S. Wu, Z. Du, C.-H. Hsu, S. Fang, Q. D. Gibson, K. Watanabe, T. Taniguchi, R. J. Cava, E. Kaxiras, H.-Z. Lu, H. Lin, L. Fu, N. Gedik, and P. Jarillo-Herrero, *Nature* **565**, 337 (2019).
 [15] K. Kang, T. Li, E. Sohn, J. Shan, and K. F. Mak, *Nature Materials* **18**, 324 (2019).

- [16] S.-Y. Xu, Q. Ma, H. Shen, V. Fatemi, S. Wu, T.-R. Chang, G. Chang, A. M. M. Valdivia, C.-K. Chan, Q. D. Gibson, J. Zhou, Z. Liu, K. Watanabe, T. Taniguchi, H. Lin, R. J. Cava, L. Fu, N. Gedik, and P. Jarillo-Herrero, *Nature Physics* **14**, 900 (2018).
- [17] J. Zhou, J. Qiao, A. Bournel, and W. Zhao, *Phys. Rev. B* **99**, 60408 (2019).
- [18] D. MacNeill, G. M. Stiehl, M. H. D. Guimaraes, R. A. Buhrman, J. Park, and D. C. Ralph, *Nature Physics* **13**, 300 (2017).
- [19] C. L. Kane and E. J. Mele, *Phys. Rev. Lett.* **95**, 226801 (2005).
- [20] C. L. Kane and E. J. Mele, *Phys. Rev. Lett.* **95**, 146802 (2005).
- [21] X. Qian, J. Liu, L. Fu, and J. Li, *Science* **346**, 1344 (2014).
- [22] S. Tang, C. Zhang, D. Wong, Z. Pedramrazi, H.-Z. Tsai, C. Jia, B. Moritz, M. Claassen, H. Ryu, S. Kahn, J. Jiang, H. Yan, M. Hashimoto, D. Lu, R. G. Moore, C.-C. Hwang, C. Hwang, Z. Hussain, Y. Chen, M. M. Ugeda, Z. Liu, X. Xie, T. P. Devereaux, M. F. Crommie, S.-K. Mo, and Z.-X. Shen, *Nature Physics* **13**, 683 (2017).
- [23] Z. Fei, T. Palomaki, S. Wu, W. Zhao, X. Cai, B. Sun, P. Nguyen, J. Finney, X. Xu, and D. H. Cobden, *Nature Physics* **13**, 677 (2017).
- [24] Z.-Y. Jia, Y.-H. Song, X.-B. Li, K. Ran, P. Lu, H.-J. Zheng, X.-Y. Zhu, Z.-Q. Shi, J. Sun, J. Wen, D. Xing, and S.-C. Li, *Phys. Rev. B* **96**, 041108 (2017).
- [25] P. Chen, W. W. Pai, Y.-H. Chan, W.-L. Sun, C.-Z. Xu, D.-S. Lin, M. Y. Chou, A.-V. Fedorov, and T.-C. Chiang, *Nature Communications* **9**, 1 (2018).
- [26] S. Wu, V. Fatemi, Q. D. Gibson, K. Watanabe, T. Taniguchi, R. J. Cava, and P. Jarillo-Herrero, *Science* **359**, 76 (2018).
- [27] Y. Shi, J. Kahn, B. Niu, Z. Fei, B. Sun, X. Cai, B. A. Francisco, D. Wu, Z.-X. Shen, X. Xu, D. H. Cobden, and Y.-T. Cui, *Science Advances* **5** (2019).
- [28] C. K. Safeer, N. Ontoso, J. Ingla-Aynés, F. Herling, V. T. Pham, A. Kurzman, K. Ensslin, A. Chuvilin, I. Robredo, M. G. Vergniory, F. de Juan, L. E. Hueso, M. R. Calvo, and F. Casanova, *Nano Letters* **19**, 8758 (2019).
- [29] B. Zhao, D. Khokhriakov, Y. Zhang, H. Fu, B. Karpiak, A. M. Hoque, X. Xu, Y. Jiang, B. Yan, and S. P. Dash, *Phys. Rev. Research* **2**, 013286 (2020).
- [30] P. Song, C.-H. Hsu, G. Vignale, M. Zhao, J. Liu, Y. Deng, W. Fu, Y. Liu, Y. Zhang, H. Lin, V. M. Pereira, and K. P. Loh, *Nature Materials* **19**, 292 (2020).
- [31] J. Sinova, S. O. Valenzuela, J. Wunderlich, C. H. Back, and T. Jungwirth, *Reviews of Modern Physics* **87**, 1213 (2015).
- [32] G. Vignale, *Journal of Superconductivity and Novel Magnetism* **23**, 3 (2009).
- [33] A. Hoffmann, *IEEE Transactions on Magnetics* **49**, 5172 (2013).
- [34] M. Isasa, E. Villamor, L. E. Hueso, M. Gradhand, and F. Casanova, *Phys. Rev. B* **91**, 024402 (2015).
- [35] P. Laczkowski, Y. Fu, H. Yang, J.-C. Rojas-Sánchez, P. Noel, V. T. Pham, G. Zahnd, C. Deranlot, S. Collin, C. Bouard, P. Warin, V. Maurel, M. Chshiev, A. Marty, J.-P. Attané, A. Fert, H. Jaffrès, L. Vila, and J.-M. George, *Phys. Rev. B* **96**, 140405 (2017).
- [36] E. Sagasta, Y. Omori, S. Vélez, R. Llopis, C. Tollan, A. Chuvilin, L. E. Hueso, M. Gradhand, Y. Otani, and F. Casanova, *Phys. Rev. B* **98**, 060410 (2018).
- [37] See Supplemental Material for a detailed explanation of the tight-binding model, the DFT calculations, the set-up for the Landauer-Büttiker and Kubo-Bastin simulations, the derivation of Eq. (2), the spin transport for in-gap states, the results for the $1T'$ phase, and the modeling of the experimental detection of the oblique SHE.
- [38] As the distinction between these two structures becomes (at least adiabatically) inconsequential in monolayers, we will not refer to it explicitly in the remainder of the text.
- [39] L.-k. Shi and J. C. W. Song, *Phys. Rev. B* **99**, 035403 (2019).
- [40] C. W. Groth, M. Wimmer, A. R. Akhmerov, and X. Waintal, *New J. Phys.* **16**, 063065 (2014).
- [41] M. Johnson and R. H. Silsbee, *Phys. Rev. Lett.* **55**, 1790 (1985).
- [42] F. Jedema, H. Heersche, A. Filip, J. Baselmans, and B. Van Wees, *Nature* **416**, 713 (2002).
- [43] J. Fabian, A. Matos-Abiaguea, P. Ertler, C. Snd Stano, and I. Žutić, *Acta Phys. Slovaca* **57**, 565 (2007).
- [44] M. Vila, J. H. Garcia, A. W. Cummings, S. R. Power, C. W. Groth, X. Waintal, and S. Roche, *Phys. Rev. Lett.* **124**, 196602 (2020).
- [45] J. Sinova, D. Culcer, Q. Niu, N. A. Sinitsyn, T. Jungwirth, and A. H. MacDonald, *Phys. Rev. Lett.* **92**, 126603 (2004).
- [46] T. Tanaka, H. Kontani, M. Naito, T. Naito, D. S. Hirashima, K. Yamada, and J. Inoue, *Phys. Rev. B* **77**, 165117 (2008).
- [47] K. Roy, *Phys. Rev. B* **96**, 174432 (2017).
- [48] L. A. Benítez, W. Saverio Torres, J. F. Sierra, M. Timmermans, J. H. Garcia, S. Roche, M. V. Costache, and S. O. Valenzuela, *Nature Materials* **19**, 170 (2020).
- [49] W. Saverio Torres, J. F. Sierra, L. A. Benítez, F. Bonell, M. V. Costache, and S. O. Valenzuela, *2D Mater.* **4**, 041008 (2017).
- [50] C. K. Safeer, J. Ingla-Aynés, F. Herling, J. H. Garcia, M. Vila, N. Ontoso, M. R. Calvo, S. Roche, L. E. Hueso, and F. Casanova, *Nano Letters* **19**, 1074 (2019).
- [51] T. S. Ghiasi, A. A. Kaverzin, P. J. Blah, and B. J. van Wees, *Nano Lett.* **19**, 5959 (2019).
- [52] In experiments, R_{ISHE} also depends on the TMD's electrical resistance [37] and the Fermi level, as seen in Fig. 3. Tunneling barriers between graphene and the TMD can suppress the spin sink effect and cause a more distributed spin absorption across the TMD width, in which case the observed signal might be partially reduced.
- [53] D. A. Abanin, A. V. Shytov, L. S. Levitov, and B. I. Halperin, *Phys. Rev. B* **79**, 035304 (2009).
- [54] E. M. Hankiewicz, L. W. Molenkamp, T. Jungwirth, and J. Sinova, *Phys. Rev. B* **70**, 241301 (2004).